Supporting Information

Moving Binary-Color Heterojunction for Spatiotemporal Multi-Level Encryption *via* Directional Swelling and Anion Exchange

*Yang Liu†, Yong Zhang†‡**

†Department of Biomedical Engineering, Faculty of Engineering, National University of Singapore, Singapore 117583

‡NUS Graduate School for Integrative Sciences and Engineering, National University of Singapore, Singapore 117456

* Corresponding author: biezy@nus.edu.sg

RESULTS

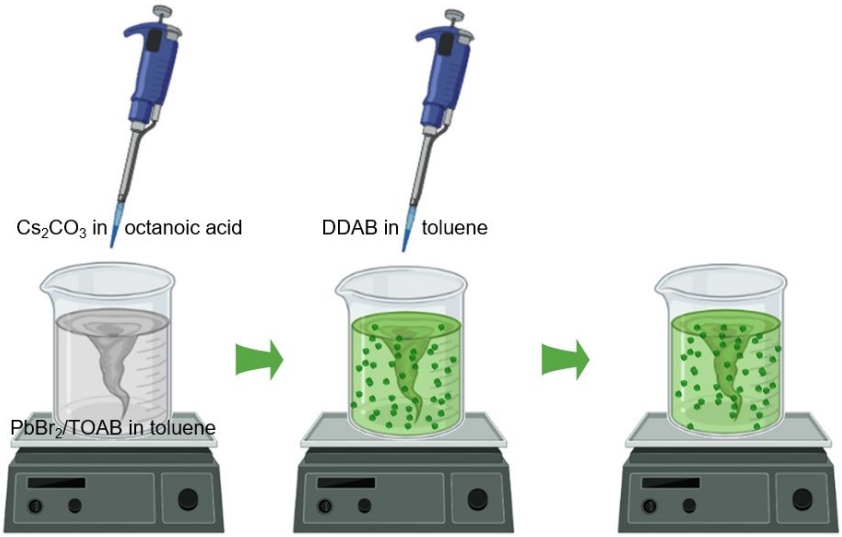

Figure S1. Schematic illustrating the room-temperature synthesis of perovskite QDs. More details, please see methods.

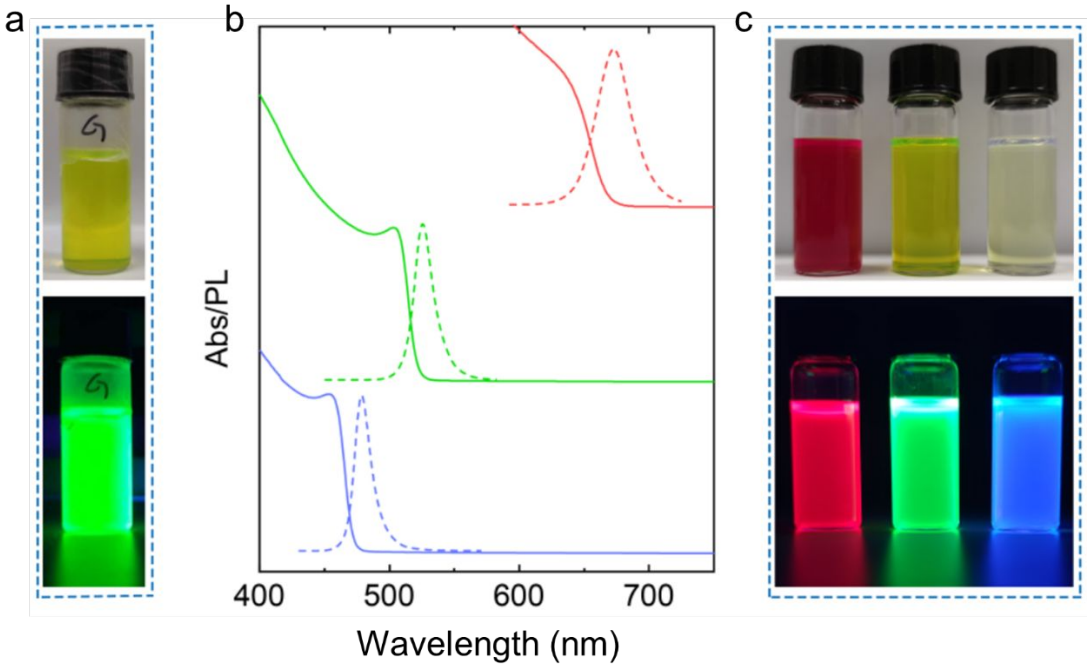

Figure S2. Optical properties of PQD. (a) Photograph under daylight and UV light of PQD in hexane after being stored for 4 weeks. (b) Typical absorption/PL spectra, and (c) photographs under daylight and UV light of red, green, and blue PQD in hexane. The red and blue PQD in hexane are obtained by ion exchange.

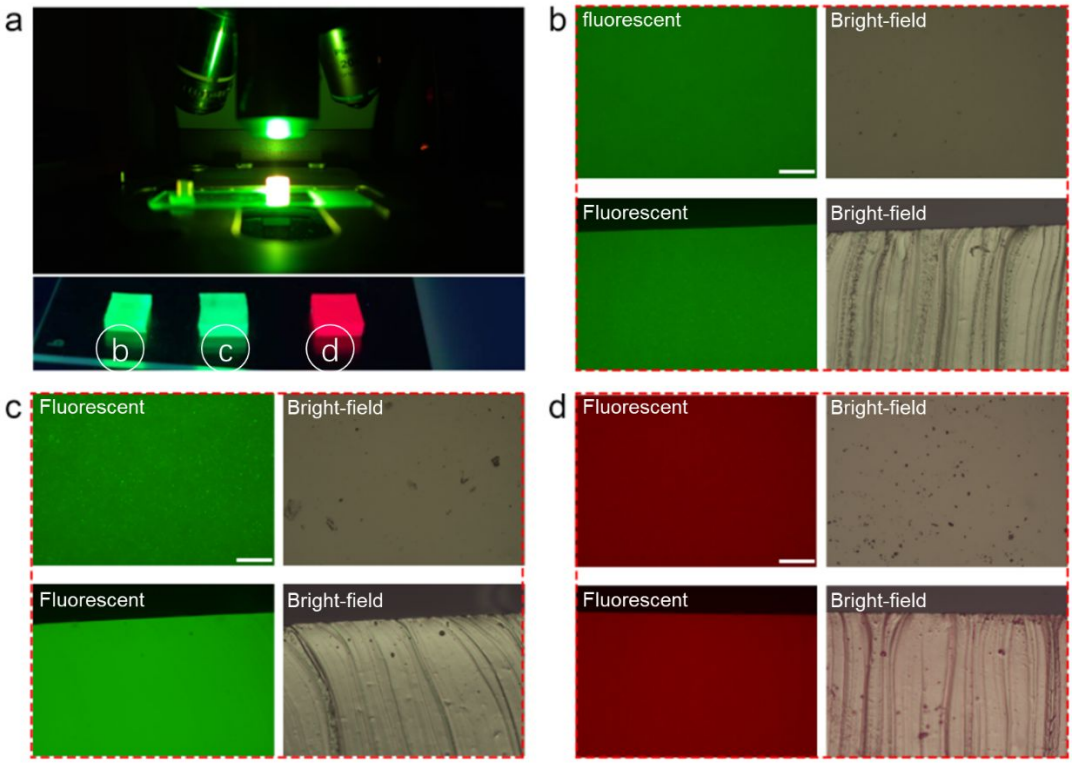

Figure S3. Microscopic images. (a) Photographs of the testing process and samples b-d. Fluorescent and bright-field images of PDMS/PQD matrix (b) before swelling, (c) after swelling in nonpolar solvents, and (d) after ion-exchange. In Figure S3b-d, top images correspond to the upper surface of the samples formed during crosslinking, whereas bottom images correspond to the lateral surface by mechanical cutting.

Strong fluorescence emission of $CsPbBr_3$ PQD is well maintained after PDMS crosslinking. First, a certain amount of DDAB can improve the stability $CsPbBr_3$ QDs.[1-2] Second, hydrophobic polymer matrices with compact molecular chains could effectively encapsulate PQDs and improve their stability in heating and humid environment;[3] the crosslinking temperature of 75 ℃ fails to damage the PQDs according to our results (PL and XRD data) and previous works have used similar crosslinking temperature to form PQD/PDMS film.[4-5] Finally, $CsPbBr_3$ QDs with cubic-tetragonal or orthorhombic show similar optical properties,[6] which is beneficial for our experiment.

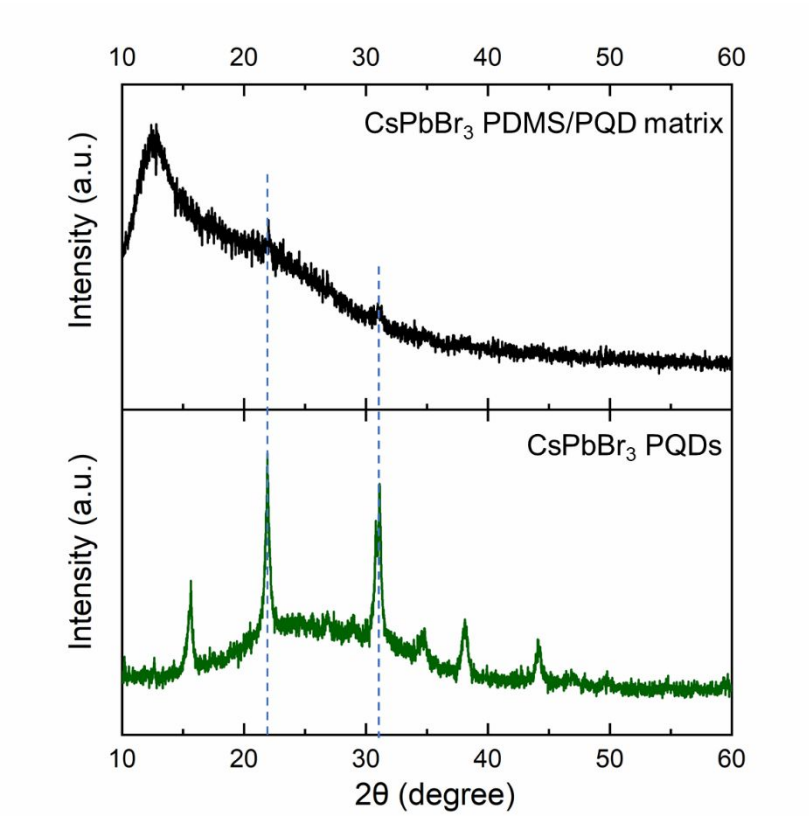

Figure S4. X-ray diffraction curve of PQD and PDMS/PQD matrix.

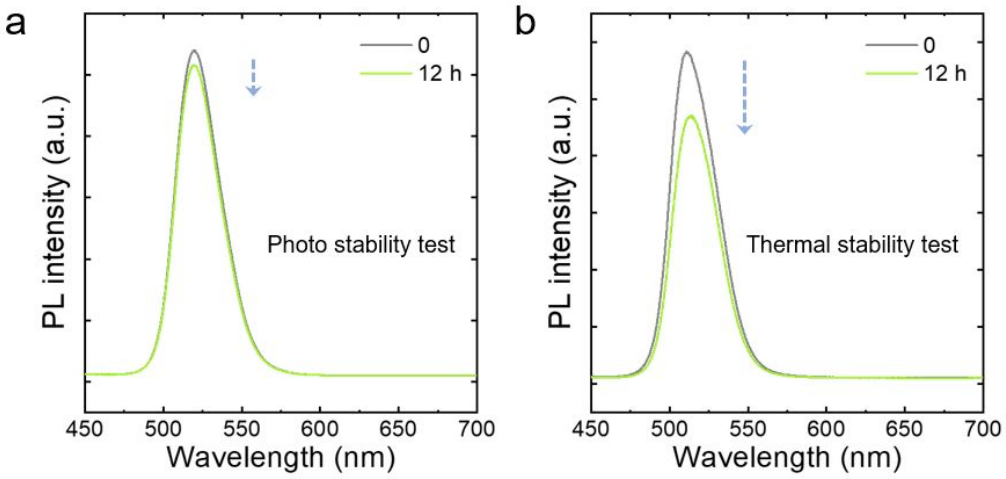

Figure S5. Photo stability test (a) and thermal stability test (b) of PQD/PDMS. The PL intensity for photo stability test was conducted by continuous UV irradiation of a portable lamp (365 nm, 6 W). The thermal stability test was by continuous heating at 70 ℃.

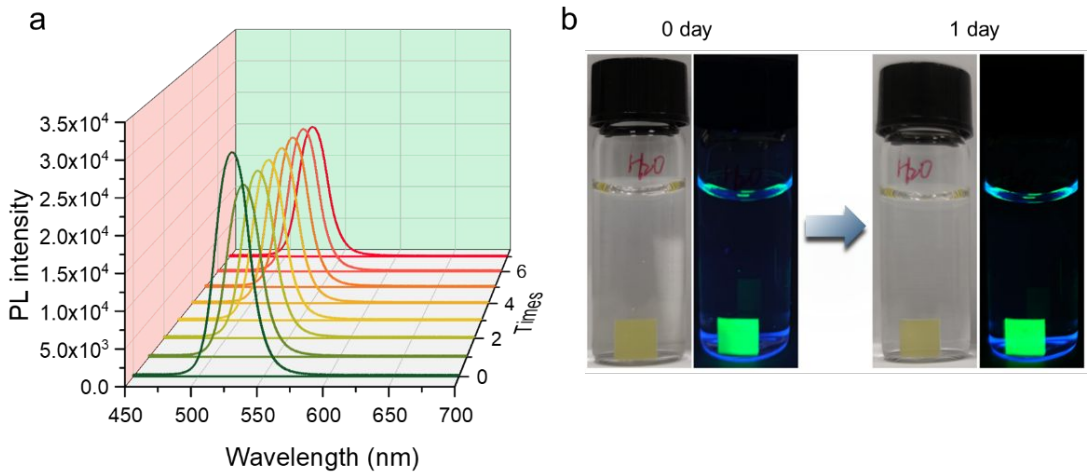

Figure S6. Stability test of PDMS/PQD matrix in pure water. (a) Time-dependent PL spectra in 1 day. (b) Photos taken under daylight and fluorescent light.

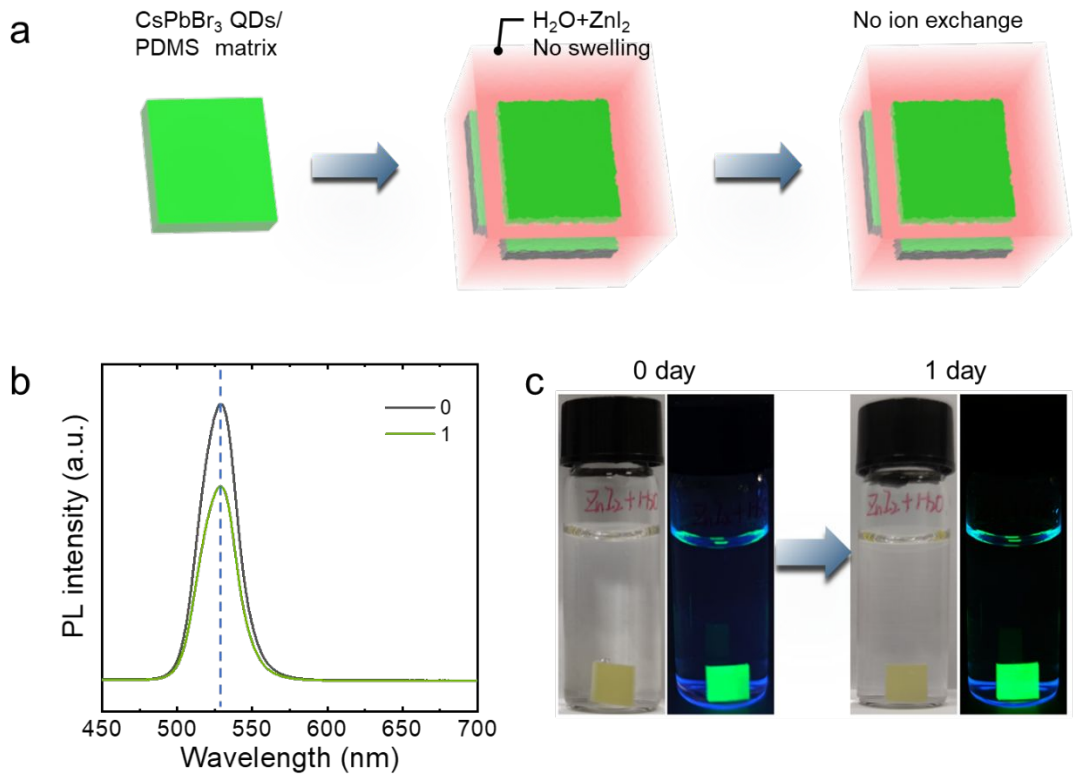

Figure S7. Ion-exchange test of PDMS/PQD matrix in ZnI_2/water (5 mg/mL). (a) schematics. (b) Time-dependent PL spectra in 1 day. (c) Daylight and fluorescent photographs.

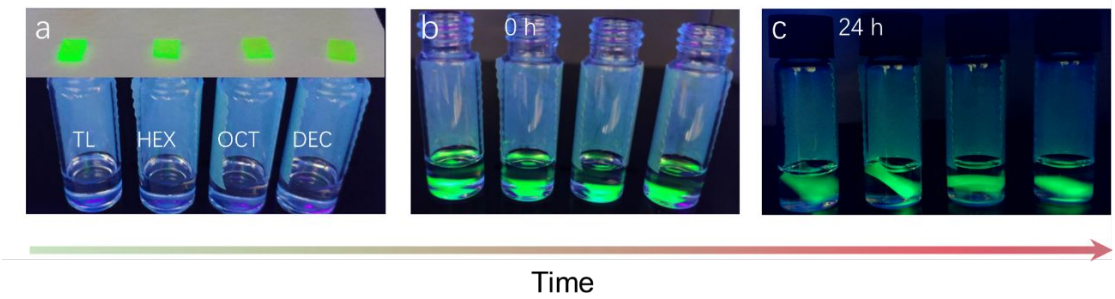

Figure S8. Swelling property of crosslinked PDMS/PQD matrixes in different solvents to swell it. (a) PDMS/PQD matrixes and solvents (TL, HEX, OCT, and DEC from left to right). (b) Fluorescent images of PDMS/PQD matrixes when they are dipped into absorbing solvents. (c) Fluorescent images 24 h later.

The result demonstrates that PQD with an average size of more than 10 nm do not leak from the PDMS network during the swelling process. The PDMS/PQD matrixes are stable in these nonpolar solvents.

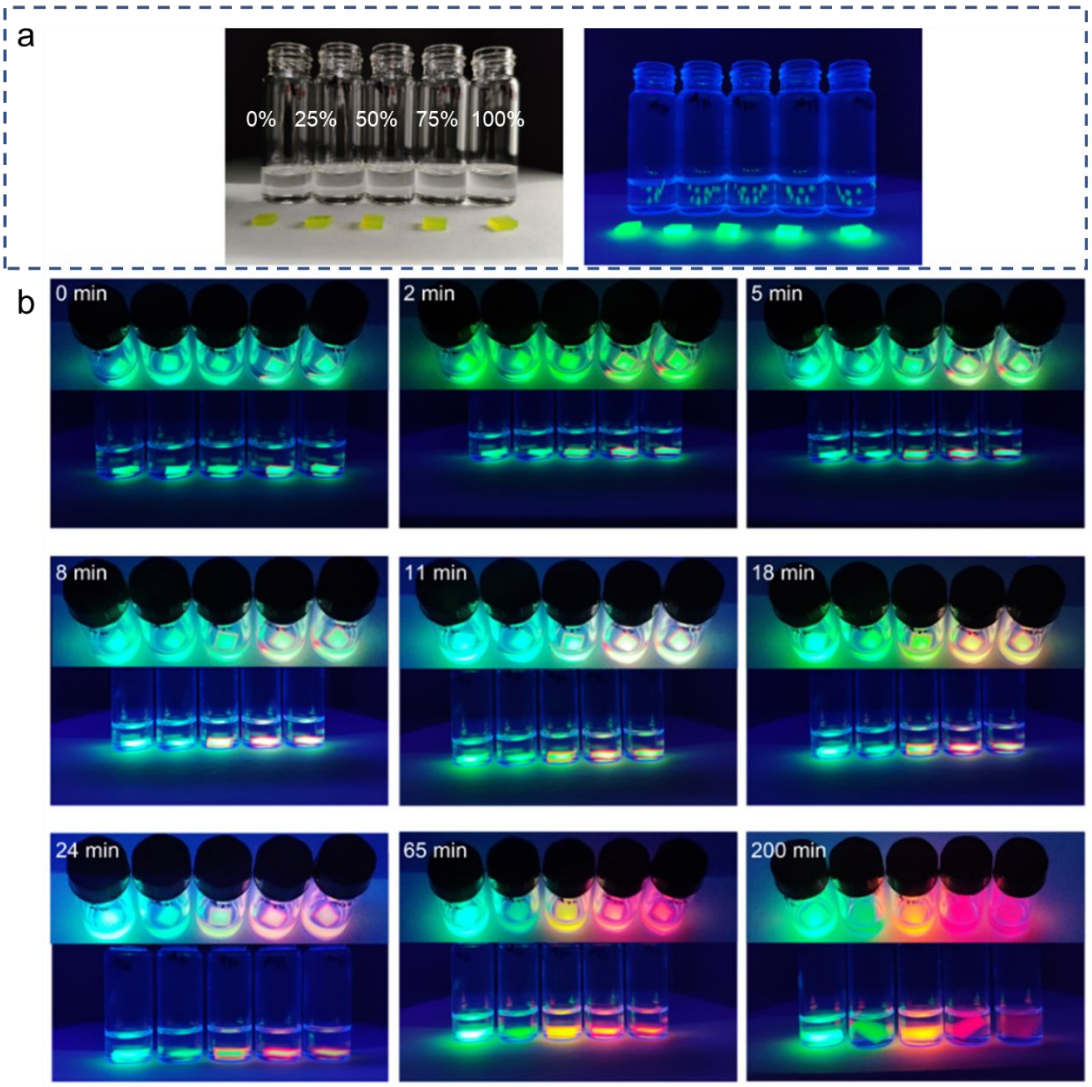

Figure S9. (a) Daylight and fluorescent images of PDMS/PQD matrix and solution with different ratio of ZnI_2 and $ZnBr_2$ (the weight ratio of ZnI_2 in mixture is 0%, 25%, 50%, 75%, and 100%). 50 μL **OAm**-assisted ion-exchange solution was added per 1 mL hexane. (b) Time-dependent fluorescent photographs of PDMS/PQD matrix after being dipped in ion-exchange solution.

After partial substitution of Br^- by I^- for PDMS/PQD matrix in OAm-assisted solution (the weight ratio of ZnI_2 in the mixture is 25% and 50%), the emission located in the yellow region is very bright. This indicated that the blurred interface or distinct intermediate transition region with yellow color is attributed to the high fluorescence of partial-doped $CsPbBr_{3-x}I_x$QDs during the directional swelling process.

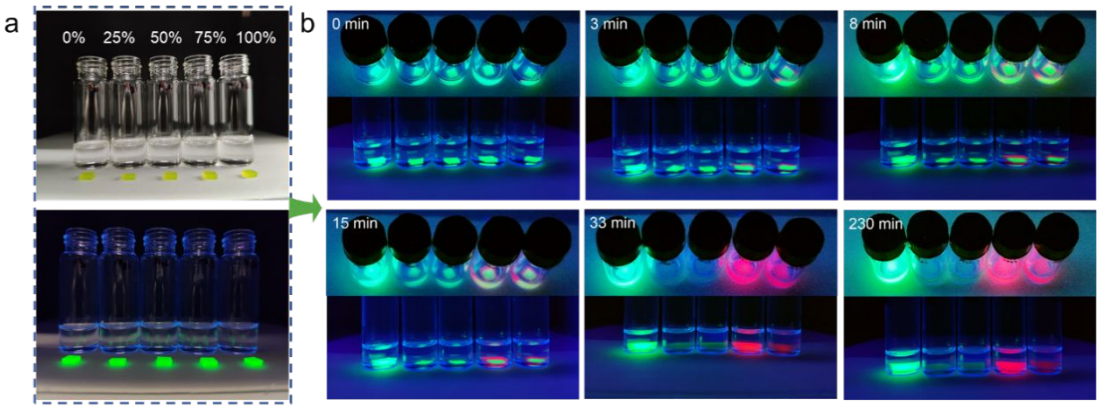

Figure S10. (a) Daylight and fluorescent images of PDMS/PQD matrix and solution with different ratio of ZnI_2 and $ZnBr_2$ (the weight ratio of ZnI_2 in mixture is 0%, 25%, 50%, 75%, and 100%). 50 μL **TOP**-assisted ion-exchange solution was added per 1 mL hexane. (b) Time-dependent fluorescent photographs of PDMS/PQD matrix after being dipped in ion-exchange solution.

After partial substitution of Br^- by I^- for PDMS/PQD matrix in TOP-assisted solution (the weight ratio of ZnI_2 in the mixture is 25% and 50%), the emission located in the yellow region is very weak. This indicated that the distinct red-green interface is attributed to the low fluorescence of partial-doped $CsPbBr_{3-x}I_x$QDs during the directional swelling process. Since the weak yellow fluorescence is liable to be fully absorbed by the red perovskite QDs in the surface of the PDMS matrix, yellow emission fails to be seen in the fluorescent spectra in Figure 2b,c.

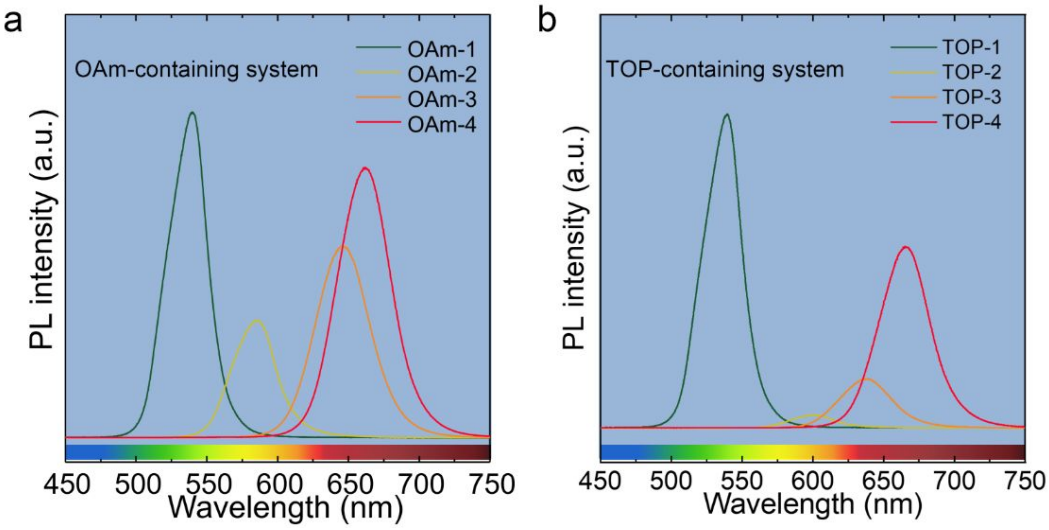

Figure S11. Fluorescence spectra of (a) OAm-containing and (b) TOP-containing ion-exchange system with different ratio of ZnI_2 (the weight ratio of ZnI_2 increase from sample 1 to sample 4) after total ion exchange.

The yellow emission for homogeneous PDMS/PQD matrix with partial substitution of Br^- by I^- in TOP-assisted solution is not fully eliminated. To further demonstrate this, we added the fluorescence spectra of OAm-containing and TOP-containing ion-exchange system with different ratio of ZnI_2 (the weight ratio of ZnI_2 increase from sample 1 to sample 4) in the Figure S11 as follows (fluorescent images located in Figure S9 and S10). For TOP-containing ion-exchange system, the emission located in the yellow region exists (Figure S11b); and the yellow emission is much weaker when compared with those of the bright red and green samples (and also the yellow emission of the OAm-containing system in Figure S11a). Since the weak yellow fluorescence of TOP-containing system is liable to be fully absorbed by the red perovskite QDs in the surface of the PDMS matrix (Figure 2c), the yellow emission fails to be seen in the fluorescent spectra in Figure 2g-i and a red-green heterojunction with distinct and higher-contrast interface forms.

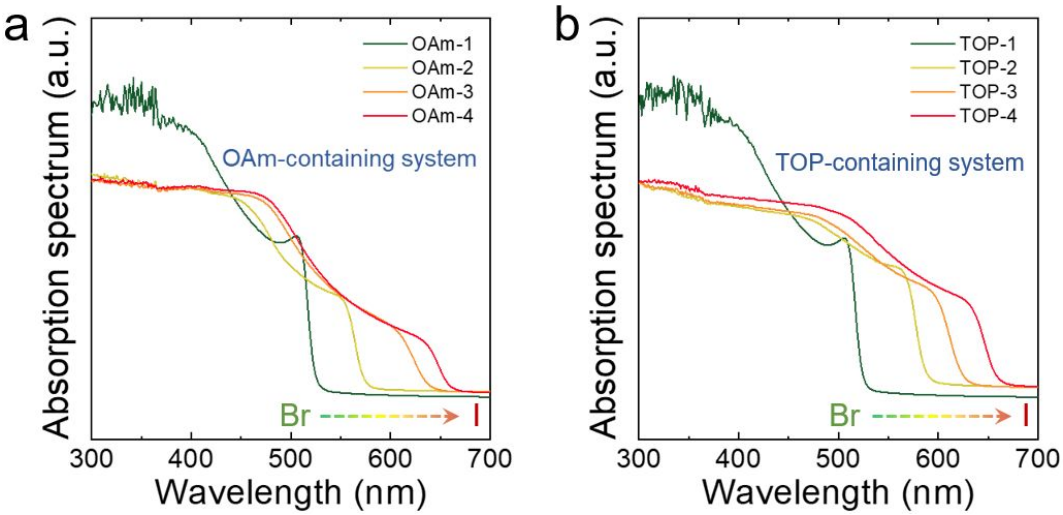

Figure S12. Absorption spectra of (a) OAm-containing and (b) TOP-containing ion-exchange system with different ratio of ZnI_2 (the weight ratio of ZnI_2 increase from sample 1 to sample 4). The weak yellow state for the TOP-containing system shows similar absorption spectra with those of the OAm-containing system, implying less efficiency in PLQY.

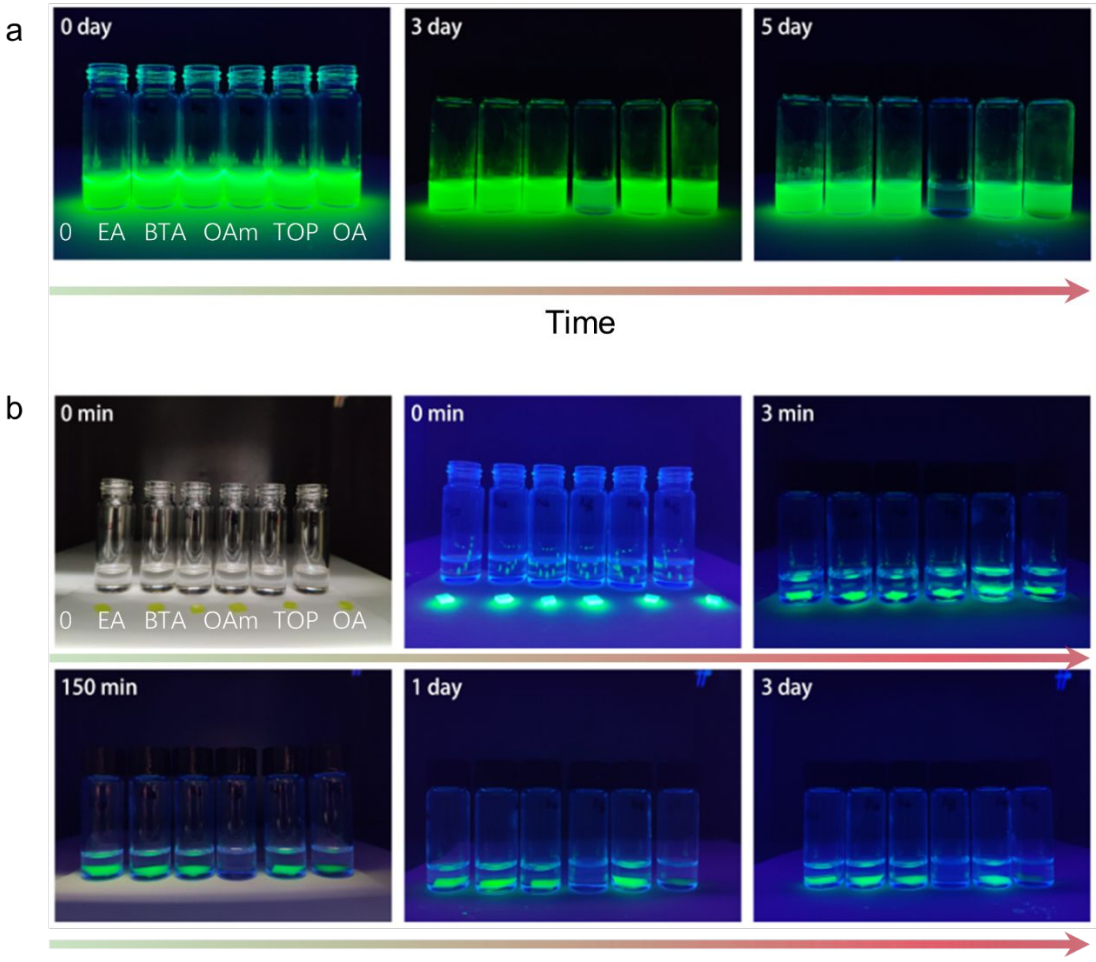

Figure S13. (a) Time-dependent fluorescent photographs of PQD in hexane after adding different cosolvents (0, EA, BTA, OAm, TOP, and OA from left to right). (b) Time-dependent fluorescent photographs of PDMS/PQD matrix after being dipped into ZnI_2 solution with different cosolvents. 50 μL of these cosolvents were added per 1 mL hexane. The left one was added 50 ul hexane as a control experiment.

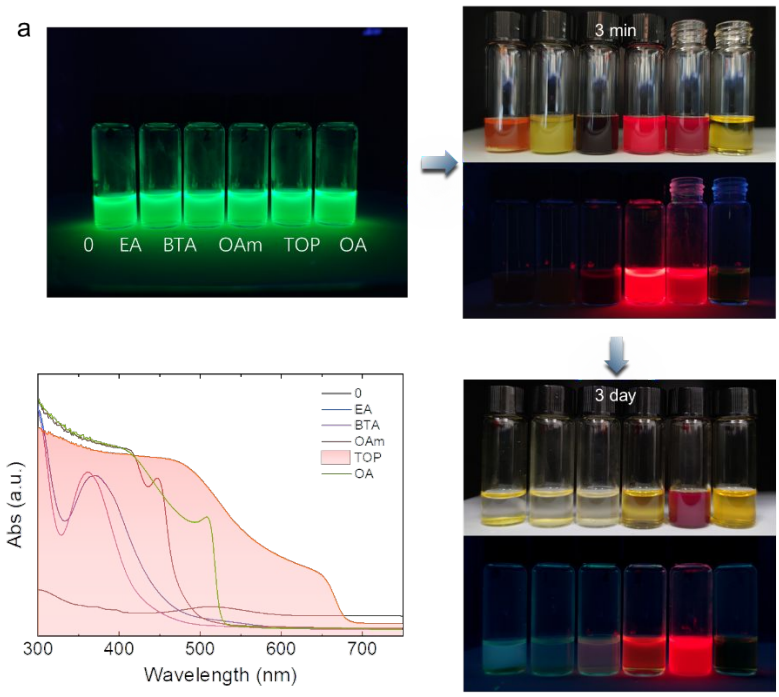

Figure S14. (a) Time-dependent fluorescent photographs of PQD in hexane after adding ZnI_2 solution with different cosolvents (0, EA, BTA, OAm, TOP, and OA from left to right). 50 μL ZnI_2 solution with cosolvent were added per 1 mL hexane. The ZnI_2 solution was at a concentration of 10 mg/mL. The left one was added moderate ZnI_2 power as a control experiment. (b) Absorption spectra 3 days later.

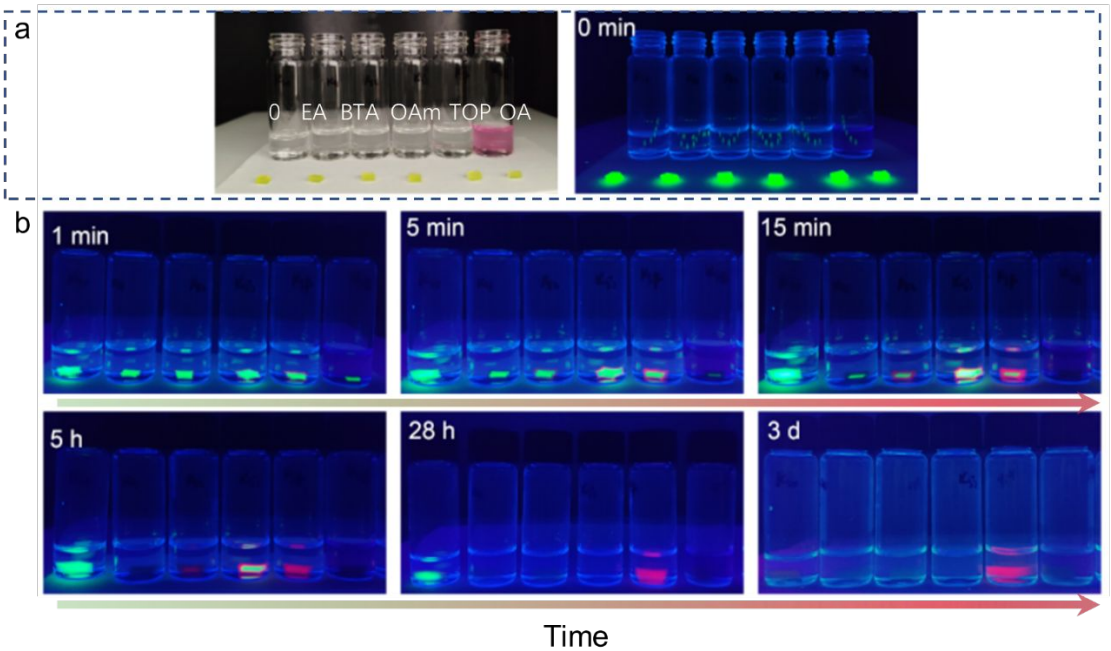

Figure S15. (a) Daylight and fluorescent images of PDMS/PQD matrix and hexane after adding ZnI_2 solution with different cosolvents (0, EA, BTA, OAm, TOP, and OA from left to right). 50 μL ZnI_2 solution were added per 1 mL hexane. The left one was added moderate ZnI_2 power as a control experiment. (b) Time-dependent fluorescent photographs of PDMS/PQD matrix after being dipped into these solutions.

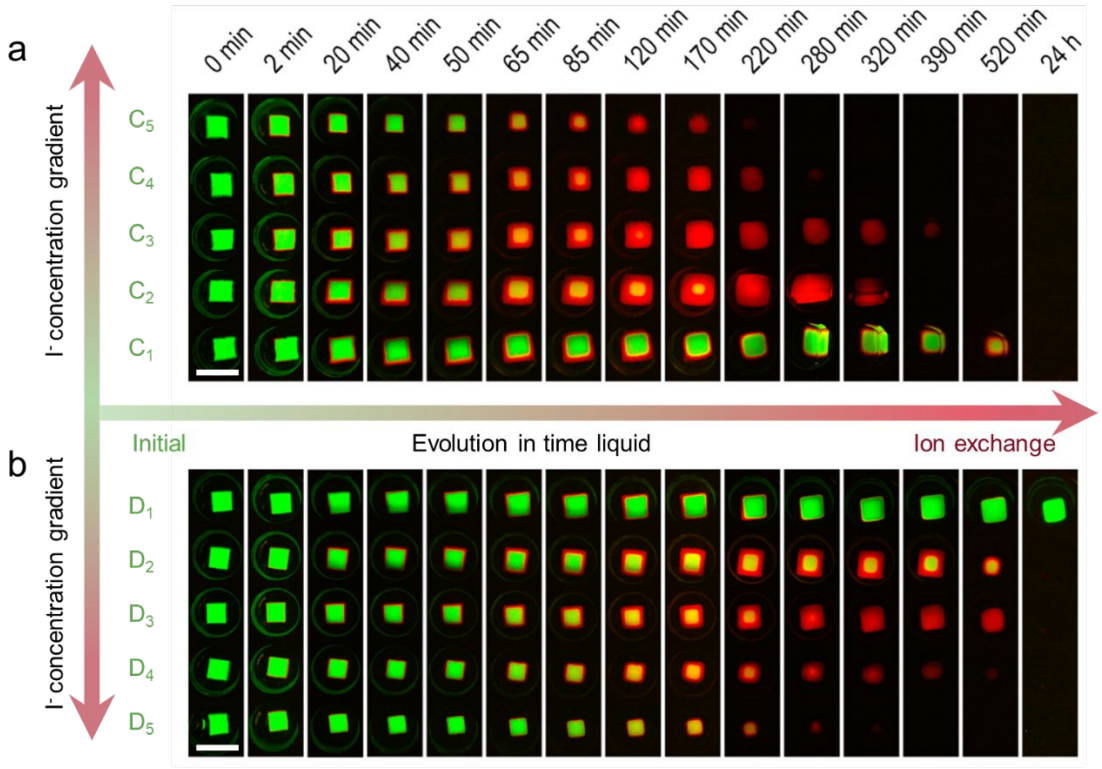

Figure S16. Time-dependent fluorescence images for PDMS/PQD matrix in OAm-assisted solution. We tried to tailor the ion-exchange rate by the ion concentration gradient and the swelling ratio. (a) In DEC and (b) mixed solvent of DEC and ODE (volume ratio of 1:1). The scale bar is 10 mm. Samples X_1-X_5 (X=C, D) correspond to time liquids with 10, 20, 30, 60, and 90 μL ion-exchange solution per 1 mL solvent.

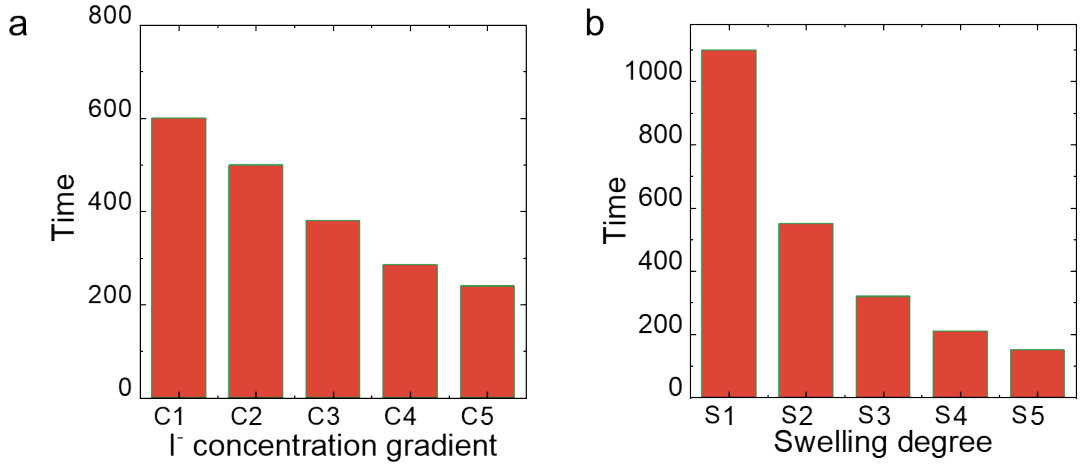

Figure S17. Total time needed to change from green to full red for samples C1-C5 and S1-S5 in Figure 3.

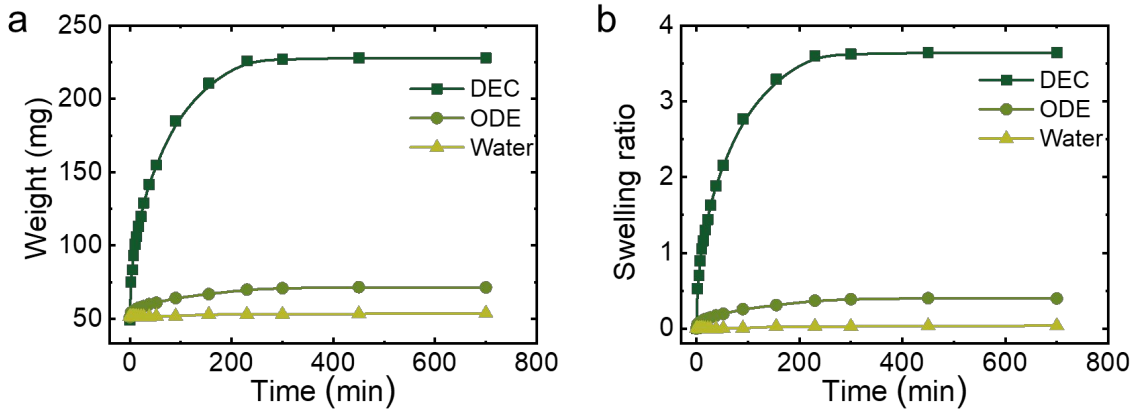

Figure S18. Swelling curves of PDMS/PQD matrix in different solvents including DEC, ODE, and water. Real-time curves of (a) weight and (b) corresponding swelling ratio. Swelling ratio (S_r) of PDMS/PQD matrix in DEC and ODE are 0.4 and 3.6, respectively. The S_r of PDMS/PQD matrix in pure water is about 0, which explains its stability in water.

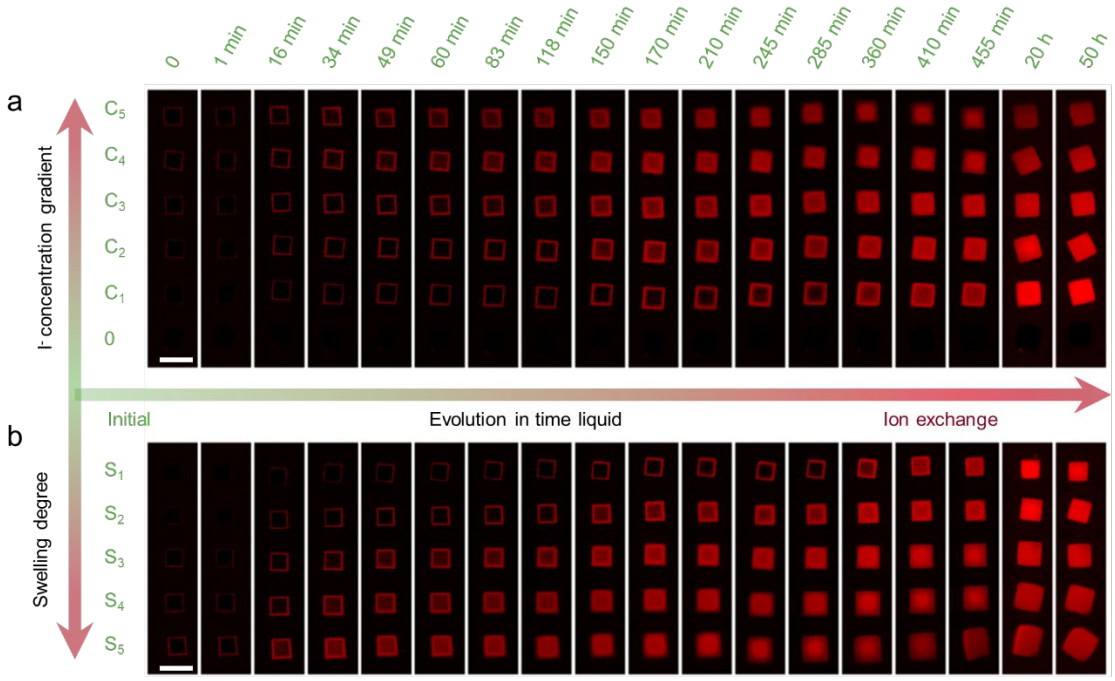

Figure S19. Extracted red part of PL images (corresponding to Figure 3) by the tailoring ion-exchange rate *via* (a) ion concentration gradient and (b) swelling ratio of PDMS in nonpolar solvents. The scale bar is set to 10 mm.

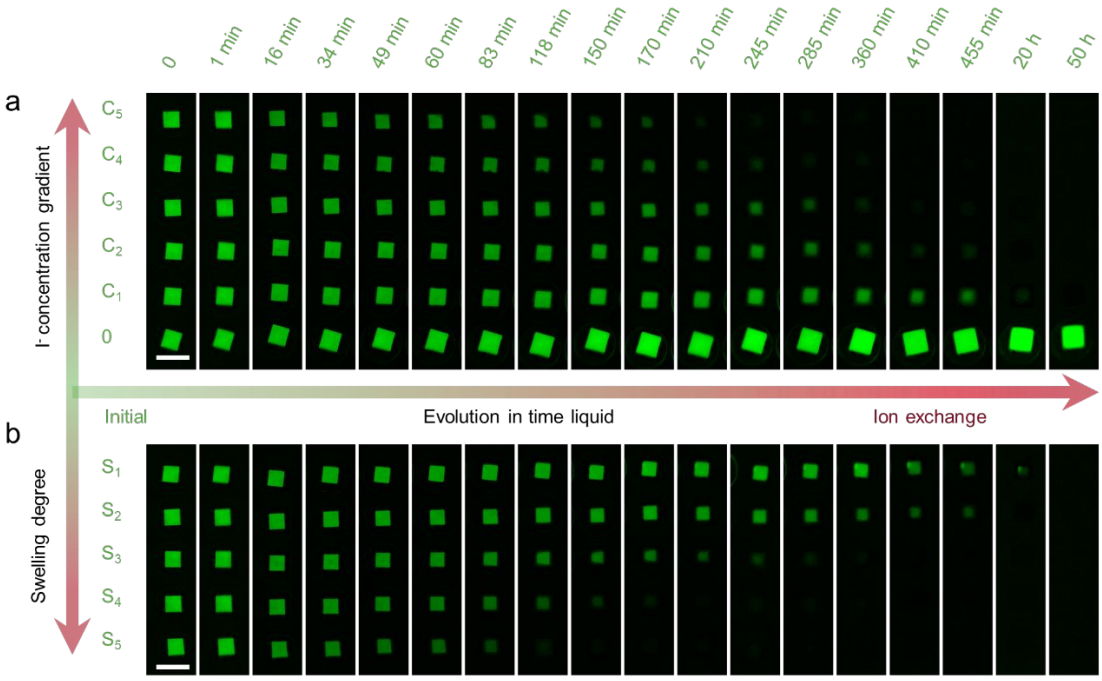

Figure S20. Extracted green part of PL images (corresponding to Figure 3) by the tailoring ion-exchange rate *via* (a) ion concentration gradient and (b) swelling ratio of PDMS in nonpolar solvents. The scale bar is set to 10 mm.

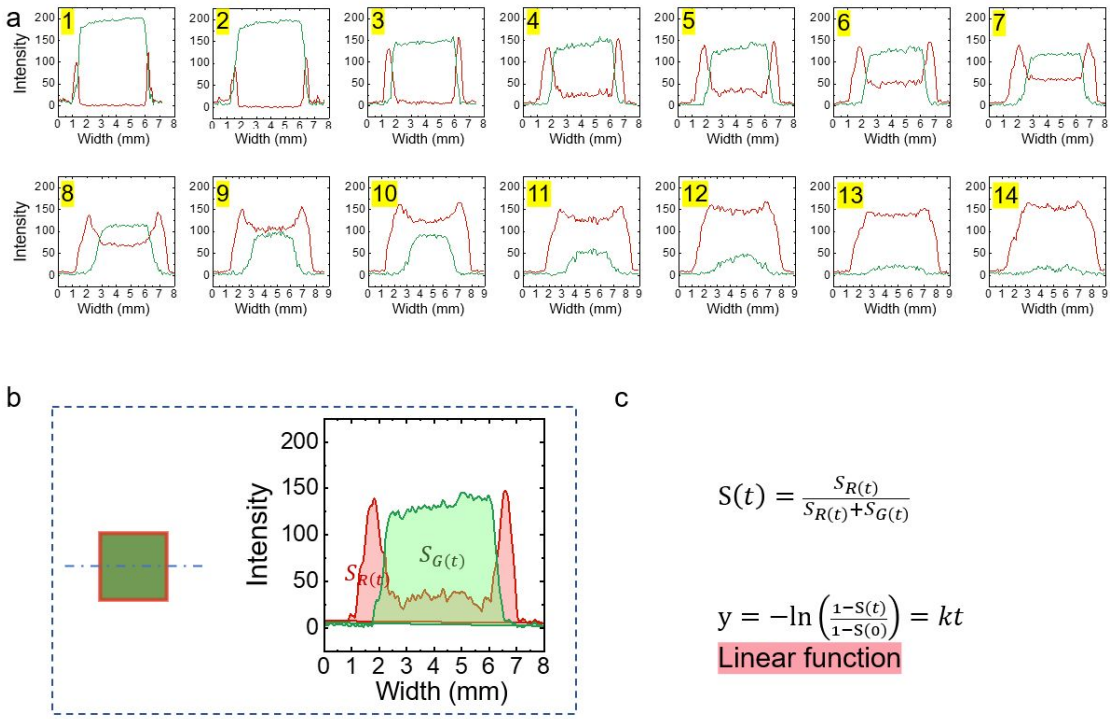

Figure S21. Quantification of dynamic red-green heterojunction during ion-exchange. (a) The profile of red and green component of the fluorescent photographs (take sample C4 in Figure 3 from left to right as an example). The color component of the emission can be resolved by red and green acquisition, which mimics how human perceive color. (b) The integral areas of the red and green profile are defined as $S_{R(t)}$ and $S_{G(t)}$. (c) Quantification of coloration rate by linear fittings.

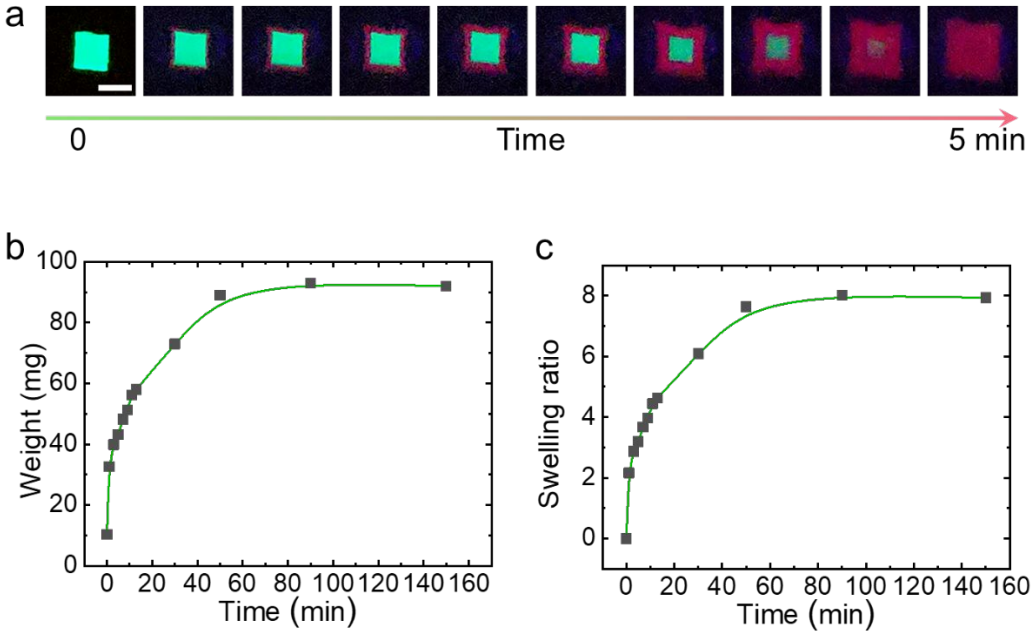

Figure S22. (a) Real-time fluorescence images of the heterojunction during ion exchange in hexane. The scale bar is 3 mm. Real-time swelling curves of (b) weight and (c) corresponding swelling ratio for PDMS/PQD matrix in hexane. The thickness of PDMS square is about 0.6 times of the samples in the Figure 2-5. The ratio of silicone elastomer base and curing agent is 10:0.8 to decrease the crosslinking ratio of PDMS. Swelling ratio (S_r) of PDMS/PQD matrix in hexane are 8, much higher than those of in DEC and ODE. The ion-exchange time can be highly reduced to several minutes by decreasing the size of PQD/PDMS squares and PDMS crosslinking ratio.

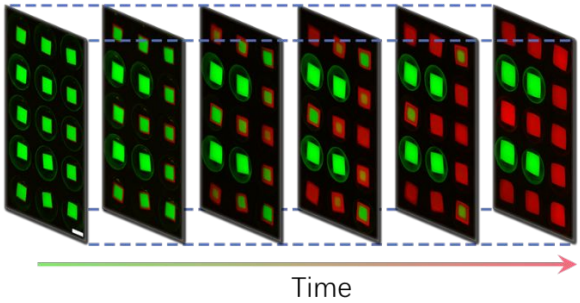

Figure S23. Fluorescent images of a time clock showing a character of “3”. The character is composed of samples with three different ion-exchange rates.

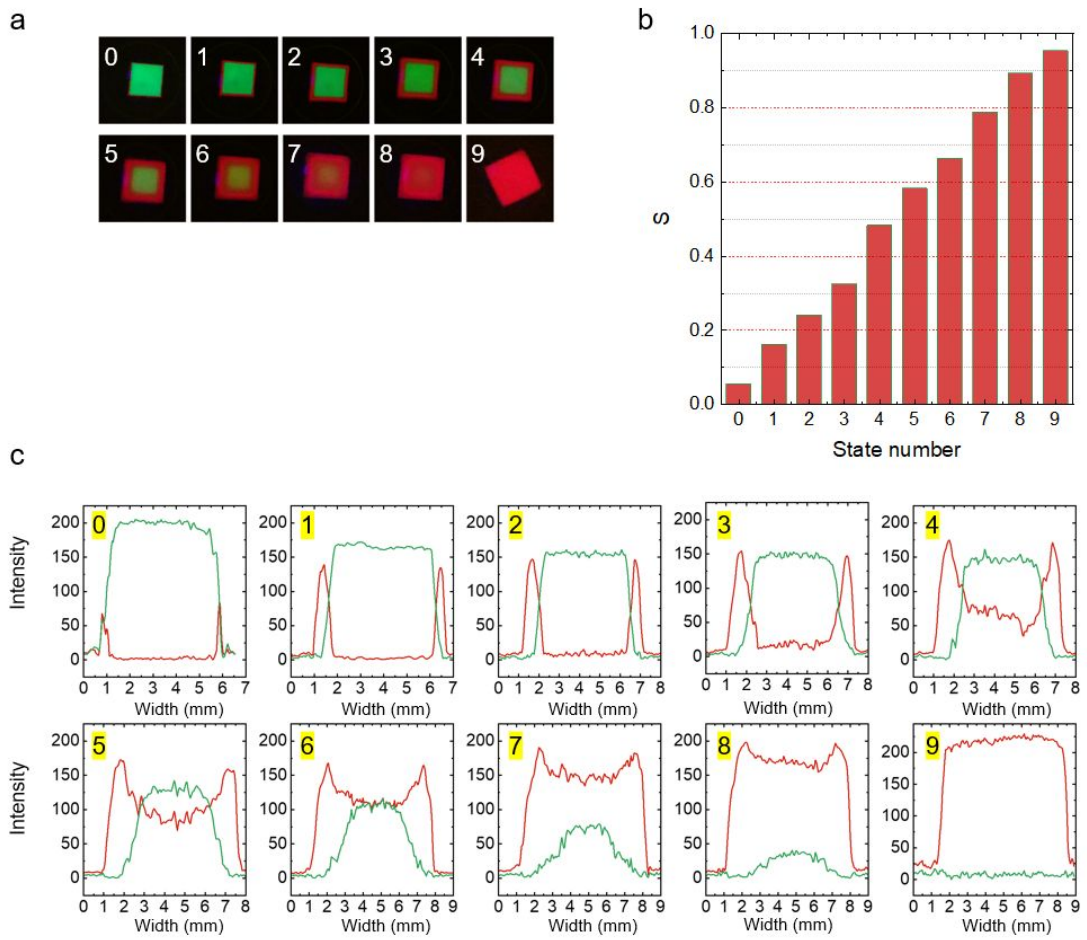

Figure S24. Ten effective states of the bicolor heterojunction during ion-exchange. (a) Selected 10 states in sample C2 in Figure 3. (b) Quantification of the 10 states by S(t). (c) The profile of the red and green components of the 10 fluorescence photographs.

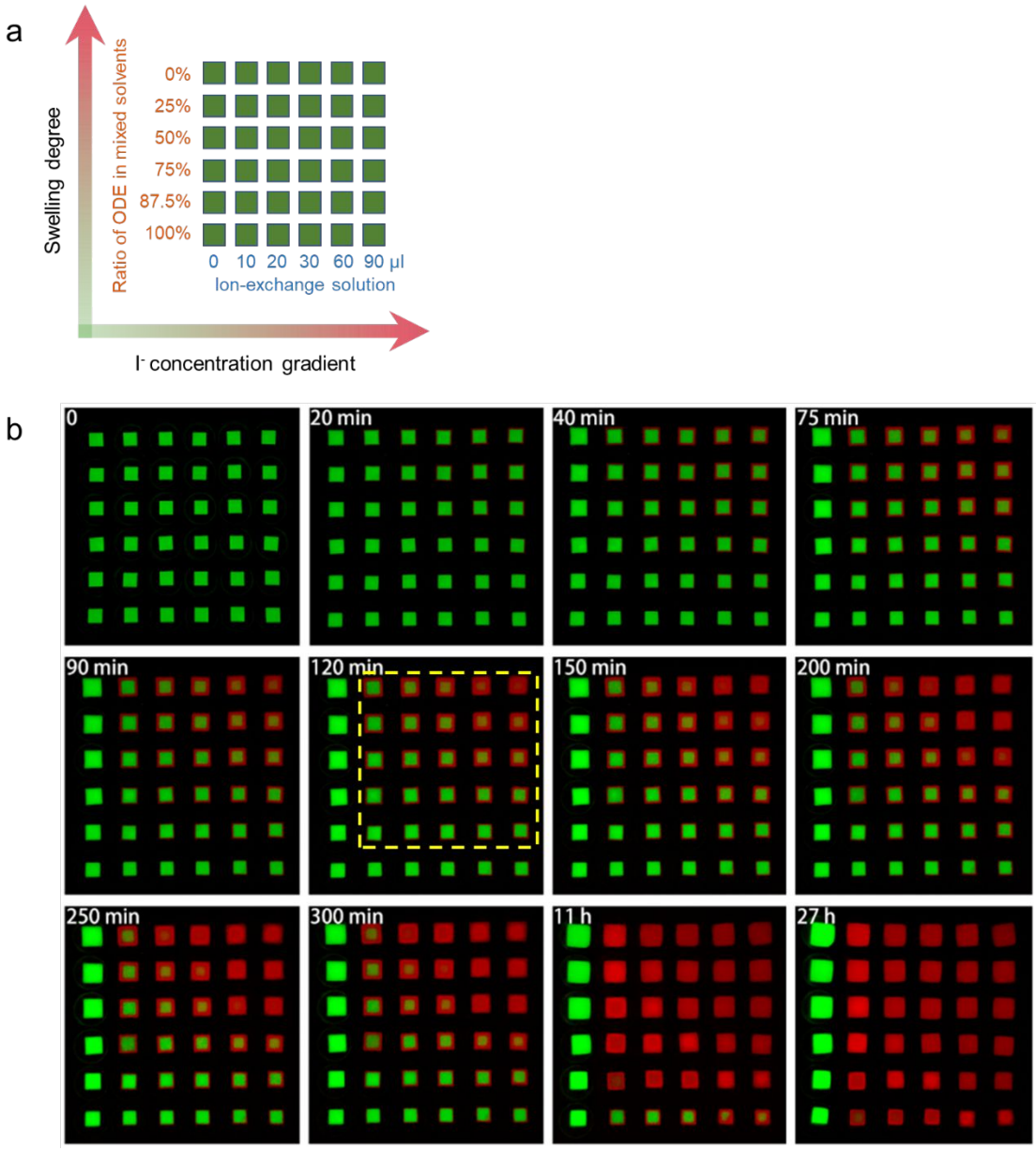

Figure S25. *In-situ* fluorescence photographs of a 6×6 array to tailor the rate of ion-exchange-induced bicolor heterojunction system in a quasi-continuous way *via* ion concentration gradient (in the horizontal direction) and swelling ratio of PDMS in nonpolar solvents (in the vertical direction). (a) Schematic and (b) fluorescent photograph by tailoring ion-exchange rate *via* ion concentration gradient and swelling ratio of PDMS nonpolar solvents.

Taking the fluorescent photograph at 120 min as an example, every red-green-heterojunction time clock has its unique operating rate, standing for its own time.

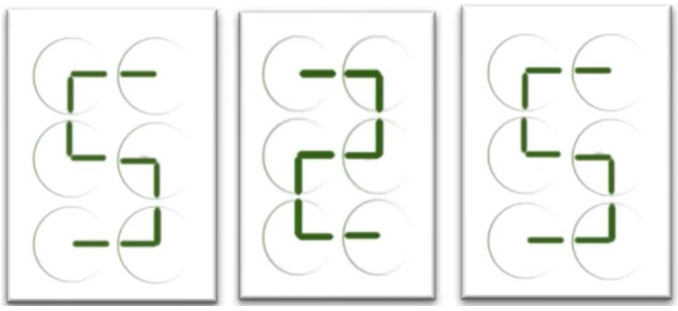

Figure S26. Encoding a digital key based on clock synchronization. Three 2×3 arrays are combined to form an anti-counterfeiting label encoded with a digital key, number '525'.

Table 1 | Calculated tunable ion-exchange rates (*K*) of samples from C1-C5 (*Kc*) to S1-S5 (*Ks*) according to the first-order fitting line (corresponding to Figure 3).

NO.	**C1**	**C2**	**C3**	**C4**	**C5**
Kc (min^{-1})	0.00214	0.00395	0.00522	0.00698	0.00894
NO.	**S1**	**S2**	**S3**	**S4**	**S5**
Ks (min^{-1})	0.00151	0.00285	0.00688	0.0129	0.0169

Table 2 | Simplified binary encryption algorithm with red and green pixels according to the ASCII-binary character table.

Character	Binary code	Encoded pixels	Character	Binary code	Encoded pixels	Character	Binary code	Encoded pixels
A	000001	🟩🟩🟩🟩🟩🟥	N	001110	🟩🟩🟥🟥🟥🟩	0	110000	🟥🟥🟩🟩🟩🟩
B	000010	🟩🟩🟩🟩🟥🟩	O	001111	🟩🟩🟥🟥🟥🟥	1	110001	🟥🟥🟩🟩🟩🟥
C	000011	🟩🟩🟩🟩🟥🟥	P	010000	🟩🟥🟩🟩🟩🟩	2	110010	🟥🟥🟩🟩🟥🟩
D	000100	🟩🟩🟩🟥🟩🟩	Q	010001	🟩🟥🟩🟩🟩🟥	3	110011	🟥🟥🟩🟩🟥🟥
E	000101	🟩🟩🟩🟥🟩🟥	R	010010	🟩🟥🟩🟩🟥🟩	4	110100	🟥🟥🟩🟥🟩🟩
F	000110	🟩🟩🟩🟥🟥🟩	S	010011	🟩🟥🟩🟩🟥🟥	5	110101	🟥🟥🟩🟥🟩🟥
G	000111	🟩🟩🟩🟥🟥🟥	T	010100	🟩🟥🟩🟥🟩🟩	6	110110	🟥🟥🟩🟥🟥🟩
H	001000	🟩🟩🟥🟩🟩🟩	U	010101	🟩🟥🟩🟥🟩🟥	7	110111	🟥🟥🟩🟥🟥🟥
I	001001	🟩🟩🟥🟩🟩🟥	V	010110	🟩🟥🟩🟥🟥🟩	8	111000	🟥🟥🟥🟩🟩🟩
J	001010	🟩🟩🟥🟩🟥🟩	W	010111	🟩🟥🟩🟥🟥🟥	9	111001	🟥🟥🟥🟩🟩🟥
K	001011	🟩🟩🟥🟩🟥🟥	X	011000	🟩🟥🟥🟩🟩🟩			
L	001100	🟩🟩🟥🟥🟩🟩	Y	011001	🟩🟥🟥🟩🟩🟥			
M	001101	🟩🟩🟥🟥🟩🟥	Z	011010	🟩🟥🟥🟩🟥🟩			

1. Song, J.; Li, J.; Xu, L.; Li, J.; Zhang, F.; Han, B.; Shan, Q.; Zeng, H. Room-Temperature Triple-Ligand Surface Engineering Synergistically Boosts Ink Stability, Recombination Dynamics, and Charge Injection toward Eqe-11.6% Perovskite Qleds. *Adv. Mater.* **2018**, *30,* e1800764.
2. Bodnarchuk, M. I.; Boehme, S. C.; Ten Brinck, S.; Bernasconi, C.; Shynkarenko, Y.; Krieg, F.; Widmer, R.; Aeschlimann, B.; Gunther, D.; Kovalenko, M. V.; Infante, I. Rationalizing and Controlling the Surface Structure and Electronic Passivation of Cesium Lead Halide Nanocrystals. *ACS Energy Lett.* **2019**, *4,* 63-74.
3. Wei, Y.; Cheng, Z.; Lin, J. An Overview on Enhancing the Stability of Lead Halide Perovskite Quantum Dots and Their Applications in Phosphor-Converted Leds. *Chem. Soc. Rev.* **2019**, *48,* 310-350.
4. Chen, Q. S.; Wu, J.; Ou, X. Y.; Huang, B. L.; Almutlaq, J.; Zhumekenov, A. A.; Guan, X. W.; Han, S. Y.; Liang, L. L.; Yi, Z. G.; Li, J.; Xie, X. J.; Wang, Y.; Li, Y.; Fan, D. Y.; Teh, D. B. L.; All, A. H.; Mohammed, O. F.; Bakr, O. M.; Wu, T.*, et al.* All-Inorganic Perovskite Nanocrystal Scintillators. *Nature* **2018**, *561,* 88.
5. Zhihai, W.; Jiao, W.; Yanni, S.; Jun, W.; Yafei, H.; Pan, W.; Nengping, W.; Zhenfu, Z. Air-Stable All-Inorganic Perovskite Quantum Dot Inks for Multicolor Patterns and White Leds. *J. Mater. Sci.* **2019**, *54,* 6917-6929.
6. Zhang, D. D.; Eaton, S. W.; Yu, Y.; Dou, L. T.; Yang, P. D. Solution-Phase Synthesis of Cesium Lead Halide Perovskite Nanowires. *J. Am. Chem. Soc.* **2015**, *137,* 9230-9233.